

The COV-OBS.x3 geomagnetic field model & ISTerre's candidates to IGRF-14

Romain Claveau¹, Nicolas Gillet¹, Pierre-Olivier Amblard², and Christopher Finlay³

¹Univ. Grenoble Alpes, Univ. Savoie Mont Blanc, CNRS, IRD, Univ. Gustave Eiffel, ISTerre, 38000 Grenoble, France

²CNRS, Univ. Grenoble Alpes, Grenoble INP, GIPSA-lab, 38000 Grenoble, France

³DTU Space, Technical University of Denmark, Centrifugevej 356, Kongens Lyngby, Denmark

September 2024

Abstract

We present ISTerre candidate models to the 14th edition of the International Geomagnetic Reference Field (IGRF). These are based on the COV-OBS.x3 field model, which is constrained until 2024.5 by ground-based and satellite magnetic observations. The latter are incorporated as 4-monthly geomagnetic virtual observatory data. It is constructed by considering as prior information temporal cross-covariances associated with auto-regressive processes of order 3 (AR-3). It allows, in comparison with previous COV-OBS editions based on lower order processes, to mimic the cut-off in the spectral density expected for periods shorter than ≈ 2 years the Alfvén time in Earth's core. Field model coefficients are furthermore projected in time based on these correlation functions, avoiding the use of arbitrary temporal basis functions. Parameters (cut-off times and variances) defining the AR-3 correlations functions are deduced from geophysical constraints. The a priori information developed here encompasses by construction the power spectra stemming from both paleomagnetic, observatory and satellite records, statistically replicating magnetic variations over a broad range of time-scales. This formalism is exploited to forecast the field evolution, and to provide realistic uncertainties for the main field and its secular variation over the upcoming 5 years.

1 Background

We report here on the construction of the COV-OBS.x3 model, the latest edition to the COV-OBS family, from which we derive ISTerre's candidates for the 14th edition of the DGRF and IGRF (for the previous 13th edition, see Alken et al, 2021). These concern:

- The main field (MF) in 2020 (DGRF);
- The MF in 2025 (IGRF);
- The average secular variation (or SV, the rate of change of the MF) from 2025 to 2030.

As its predecessors, COV-OBS.x3 is based on ground-based and satellite magnetic observations. These are incorporated by means of virtual observatories (Hammer et al, 2021). One particularity of the COV-OBS models is to consider an a priori information in time based on stochastic processes. This approach, in contrast with regularization procedures often applied to reduce the non-uniqueness of the inverse problem, allows to derive posterior model uncertainties (Gillet et al, 2013). Previous

editions (Gillet et al, 2015; Huder et al, 2020) were based on cross-correlation functions from second order auto-regressive (or AR-2) processes. This stochastic framework has been incorporated into the construction of alternative models, such as KALMAG (Baerenzung et al, 2022) where AR-2 properties are considered instead via the advection of stochastic equation within a Kalman filter.

In this updated version we propose a significant methodological shift, by introducing third-order (or AR-3) processes in the construction of the a priori cross-covariances on Gauss coefficients. This allows to mimic the cut-off in the power spectral density (PSD) observed for short time-scales in advanced numerical simulations of the geodynamo, in link with magnetic diffusion (Aubert and Gillet, 2021). It also mitigates possible spurious variability related to external field leakage when allowing too large rapid fluctuations (Finlay et al, 2017). We also follow Hellio and Gillet (2018) and project the model parameters on the correlation functions when interpolating and extrapolating Gauss coefficients, avoiding this way the use of arbitrary B-spline functions for the temporal representation.

We start by describing in §2 the geomagnetic observations used to build the field model from which our candidate models are extracted. Next in §3 we detail the model parametrization, the derivation of the AR-3 a priori information, the inversion procedure and the interpolation/extrapolation method based on AR-3 correlation functions. In §4 we illustrate the fit to magnetic data, before we present the time evolution of the field model and define our candidate models for the DGRF (2020) and IGRF (2025) MF, as well as the SV prediction over 2025–2030.

2 Geomagnetic observations

We focus here on the satellite era (1999.5–2024.5), and consider ground observatories (GO) and geomagnetic virtual observatories (GVO). Three components GO observations are incorporated as 4-monthly SV data, in order to avoid dealing with the crustal bias. The GO 4-monthly SV time series¹ are derived from version 0140 (up to January 2024) of the ground observatory hourly means between January 1997 and April 2024 from the database AUX_OBS prepared by the British Geological Survey² (Macmillan and Olsen, 2013). Robust 4-monthly means of MF series are computed from hourly means, after subtracting predictions from the CM4 ionospheric field (Sabaka et al, 2004) and the CHAOS-7 external field (Finlay et al, 2020). This latter uses as input the *RC* index (Olsen et al, 2014). 4-monthly GO SV series are then computed as annual differences of GO MF time series.

Our model also incorporates three components MF GVO data from the CHAMP, Oersted, GRACE, CryoSat-2 and Swarm missions³ at 300 locations on an equal area grid. We refer to Hammer et al (2021) for details about the processing algorithm. For all mission but Swarm, we consider 12-monthly means, to avoid possible aliasing effects in relation with the slow drift in local time of polar orbiting satellites. Because the Swarm constellation covers local times at a higher cadence, Swarm GVO MF data are incorporated as 4-monthly means. They are derived from Swarm L1B Mag-L OPER data version 0602. Data up to end of April 2023 have been used. For each GVO dataset we consider values for observed field (uncleaned data) and for the core field (for which estimates of magnetospheric and ionospheric fields have been removed). For core field GVO data, estimates of the CIY4 ionospheric and induced fields have been removed (Sabaka et al, 2018), as well as estimates of CHAOS-7 magnetospheric and induced fields. Furthermore, a denoising has been applied to remove remaining external and toroidal terms, estimated up to spherical harmonic degree $l = 13$. In order to mitigate the impact of field-aligned currents we consider, instead of three-components observations, intensity data $F = \sqrt{B_r^2 + B_\theta^2 + B_\phi^2}$ for GVO located at dipole latitudes $|\lambda_D| > 55^\circ$.

The observation operator for the cleaned GO SV and GVO MF ("core") data is only related to our internal field model coefficients. The observation operator for the difference between observed and core field GVO data is associated with the external field model coefficients. For each site separately, uncertainty estimates $(\sigma_r, \sigma_\theta, \sigma_\phi)$ for the GO series are obtained from the misfit to the CHAOS-7 field

¹<http://www.spacecenter.dk/files/magnetic-models/GO/>

²ftp://ftp.nerc-murchison.ac.uk/geomag/Swarm/AUX_OBS/hour/

³<http://www.spacecenter.dk/files/magnetic-models/GVO/>

model. Those associated with the GVO series have been estimated from the misfit to the contributing satellite and ground-based data (see Barrois et al, 2018). Uncertainties on F data are obtained by propagating the three components errors as $\sigma_F = \frac{|B_r|}{F}\sigma_r + \frac{|B_\theta|}{F}\sigma_\theta + \frac{|B_\phi|}{F}\sigma_\phi$. Since we get rid of the projection onto splines with 2 yr knots spacing, we do not add on top of these observation errors the modeling errors considered by Huder et al (2020) for the construction of COV-OBS.x2. We show in Fig. 1 histograms for the observation error. These are generally lower on the ϕ component, the less affected by external signals. It is as low as ≈ 1.3 nT for CHAMP or CryoSat, and 1.15 nT for Swarm. This is to be compared with an uncertainty level closer to 2 nT along θ , and larger than 2.3 nT for B_r . Uncertainties for GVO based on platform magnetometers (Kloss et al, 2021) are significantly larger for GRACE, while for CryoSat-2 they are closer to error levels from dedicated magnetic missions.

3 Parameterization and inversion process

3.1 Model parametrization

The parameterization and methodology for COV-OBS.x3 only partly relies on the procedures described for previous versions (Gillet et al, 2013, 2015; Huder et al, 2020). We recall here the overall underlying framework and then discuss in more details the key additions to this new edition. We assume the mantle to be insulating. The magnetic field $\mathbf{B} = -\nabla V$ then derives from a potential for $r \geq c = 3485$ km, the Earth's core radius. The potential $V = V_i + V_e$ is separated between internal and external sources. The internal (core) field is expanded onto spherical harmonics as

$$V_i(r, \theta, \phi) = r_E \sum_{l=1}^L \left(\frac{r_E}{r} \right)^{l+1} \sum_{m=0}^l (g_l^m \cos(m\phi) + h_l^m \sin(m\phi)) P_l^m(\cos \theta), \quad (1)$$

with a truncation at spherical harmonic degree $L = 14$. Here $r_E = 6371.2$ km is the Earth's reference radius, (g_l^m, h_l^m) are the Schmidt semi-normalized internal Gauss coefficients, and P_l^m the associated Legendre polynomials. The external field potential

$$V_e(r, \theta, \phi) = r_E \sum_{l=1}^{L_e} \left(\frac{r}{r_E} \right)^l \sum_{m=0}^l (q_l^m \cos(m\phi) + s_l^m \sin(m\phi)) P_l^m(\cos \theta) \quad (2)$$

is restricted to a dipole aligned to the internal dipole (so $L_e = 1$), with (q_l^m, s_l^m) the Schmidt semi-normalized external Gauss coefficients. It is then described by a single coefficient \tilde{q}_1^0 , such that

$$\begin{pmatrix} q_1^0 \\ q_1^1 \\ s_1^1 \end{pmatrix} = \frac{\tilde{q}_1^0}{\sqrt{(g_1^0)^2 + (g_1^1)^2 + (h_1^1)^2}} \begin{pmatrix} g_1^0 \\ g_1^1 \\ h_1^1 \end{pmatrix}. \quad (3)$$

Contrary to previous versions of COV-OBS, we ignore fields induced in the core, because the hydro-magnetic response of the rapidly rotating fluid core is much reduced in comparison with the response of a perfect solid conductor that was considered so far (Thea Lepage, pers. comm.).

One important modification w.r.t. previous COV-OBS models concerns the temporal projection of the model coefficients. Here we get rid of the spline functions commonly used since Bloxham and Jackson (1992). The interpolation at any observation epoch is performed by projecting onto geophysically justified correlation functions, following Hellio and Gillet (2018). These functions are described in §3.2. The model inverted here is sampled every year over $[t_i, t_e] = [1999.5, 2024.5]$, so here a total of $N = 26$ epochs.

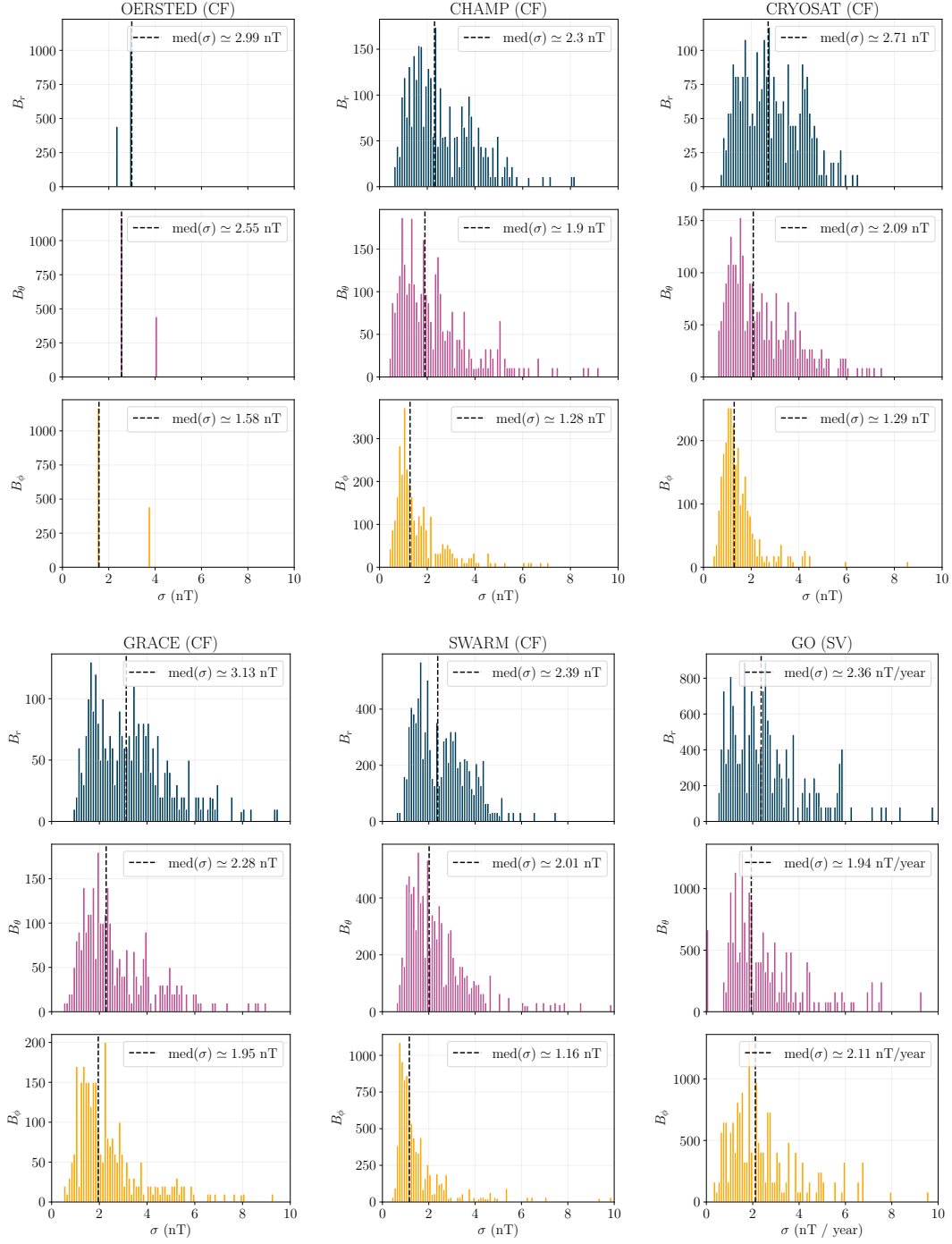


Figure 1: Histograms of the observations uncertainties considered in this study for "core" GO and GVO data. The vertical dashed line indicates the median uncertainty value. The singular distribution for Oersted is the consequence of a single star-tracker being available, rendering uncertainties dominated by attitude errors for this mission.

3.2 Stochastic priors for the Gauss coefficients

3.2.1 A priori information for the core field

In previous editions of the COV-OBS model, AR-2 processes have been considered to build the a priori temporal cross-covariances of Gauss coefficients. This was justified based on the spectral index $p = 4$ found for the PSD $S(f) \propto f^{-p}$ of the magnetic field in the range $2 \lesssim 1/f \lesssim 70$ yr, with f the frequency (Lesur et al, 2018). However, advanced numerical simulations of the geodynamo (Aubert and Gillet, 2021) indicate that $S(f)$ steepens for periods shorter than the Alfvén time T_a (≈ 2 yr in Earth’s core, see Gillet et al, 2010). The core field evolution on these time-scales is difficult to constrain, due to ambiguities between internal and external sources (e.g. Lesur et al, 2022). The projection onto spline functions with 2 yr knot spacing was hindering rapid changes in previous COV-OBS models. Shortening the knot spacing with an AR-2 prior would have led to unsatisfying leakage from unmodelled external contributions on short periods, in part because the AR-2 PSD allows too much variability on short time-scales (Finlay et al, 2017). Here we build a correlation function that accounts for the steep decay of the magnetic field PSD at high frequencies by relying on higher order (AR-3) stochastic processes (recalling that the PSD for AR- n processes behave $S(f) \propto f^{-2n}$ towards short time-scales). A linear AR-3 process $X(t)$ is governed by a stochastic equation of the form

$$X''' + a_2 X'' + a_1 X' + a_0 X = a_z Z, \quad (4)$$

where Z represent here a centered white noise of unit variance. The determination of the 4 parameters $a_{0,1,2,z}$ comes down to finding one variance and 3 time-scales, as detailed below. Our argumentation is based on the shape of the magnetic field PSD.

In order to mimic the spectrum of the core magnetic field, we aim at building a correlation function, as simple as possible, such that $S(f)$ describes 4 spectral ranges, with indices $p = 0, 2, 4$ and 6 indicating low to high frequencies. The cut-off between $p = 0$ and 2 is seen only for the axial dipole from paleomagnetic records, for a period $T_d = 2\pi/\omega_d \approx 50 - 100$ kyr (Constable and Johnson, 2005). Parameter estimations using stochastic models indicate $\omega_d^{-1} \approx 10$ kyr, in link with magnetic diffusion (Buffett and Puranam, 2017; Morzfeld and Buffett, 2019). The cut-off between $p = 4$ and 6 (actually gradually towards even steeper slopes) is seen for all coefficients in advanced geodynamo simulations, for a period shorter than the Alfvén time $T_a = 2\pi/\omega_a \approx 2$ yr, independent of the spherical harmonic degree l . The cut-off between $p = 0$ and 4 is seen for all Gauss coefficients but the axial dipole, for a period commensurate with the SV time-scale

$$\tau_{SV}(l) = \frac{\sum_{m=0}^l \sigma_{g_l^m}^2 + \sigma_{h_l^m}^2}{\sum_{m=0}^l \sigma_{\dot{g}_l^m}^2 + \sigma_{\dot{h}_l^m}^2}, \quad (5)$$

related to the vortex turn-over time (Gillet et al, 2013; Bouligand et al, 2016). We use here the notation $\sigma_{g_l^m}^2 = \mathbb{E}(g_l^{m2})$ and $\sigma_{\dot{g}_l^m}^2 = \mathbb{E}(\partial_t g_l^{m2})$ and a similar notation for the h_l^m . Lhuillier et al (2011) shows that $\tau_{SV}(l)$ (in yr) evolves approximately as $\approx 400/l$.

The above situation can be simply represented by a PSD of the form

$$S(\omega) = \frac{K}{(\omega_d^2 + \omega^2)(\omega_u^2 + \omega^2)(\omega_a^2 + \omega^2)}, \quad (6)$$

with K a constant and $\omega = 2\pi f$ the angular frequency. We show in Appendix A how to derive a correlation function associated with such a PSD. Its associated correlation function takes the simple analytical form (24). For all non-dipole coefficients, the parameters entering (6) are supposed independent of the order m , and vary only with the degree l . The axial dipole is treated separately, because of its particular behavior presenting an intermediate spectral range with index $p = 2$. We then present

in Appendix B how we determine in practice the parameters $\omega_{d,u,a}$ and the variances entering our correlation functions.

The associated PSD are illustrated in Fig. 2 for the axial dipole, and in Fig. 3 for the other coefficients. We clearly see the decrease with the degree l of the variance, as well as for the cut-off period between frequency ranges presenting a 0 and 4 spectral index. Our choice of prior for the axial dipole allows more power at intermediate frequencies, in comparison with previous editions of COV-OBS. The cut-off on short periods towards a spectral index $p = 6$ is characteristic of AR-3 processes.

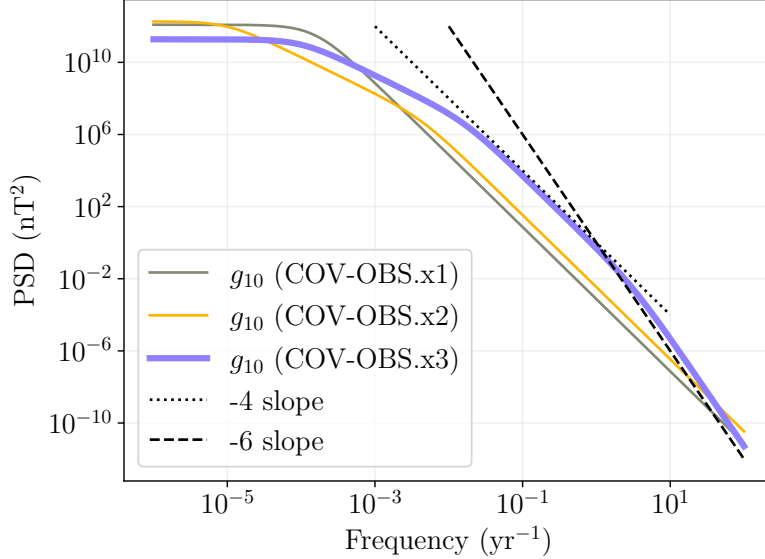


Figure 2: PSD associated with the a priori cross-correlation function considered for the axial dipole for the construction of COV-OBS.x3, compared to previous editions.

3.2.2 A priori correlation function for the external dipole field

For the external field, we do not rely on an AR-3 process but instead consider, as suggested by Huder et al (2020), the combination of an AR-1 (i.e. Laplacian) and AR-2 (or damped oscillator) correlation functions:

$$C_{\tilde{q}_1^0}(\tau) = \sigma_1^2 \exp(-\alpha_1|\tau|) + \sigma_2^2 \exp(-\alpha_2|\tau|) \left[\cos(\omega_2\tau) + \frac{\alpha_2}{\omega_2} \sin(\omega_2\tau) \right]. \quad (7)$$

In order to determine the 5 parameters (2 variances and 3 times) entering (7), we rely on the RC index for the magnetospheric activity (Olsen et al, 2014). Because we use satellite and observatory data built from annual or 4-monthly means, our estimate of \tilde{q}_1^0 cannot be considered as instantaneous, but instead as a time-average. We then build our prior on this parameter from the series $RC(t)$ over the period 1997-2024, after applying a low-pass filter with cut-off period 2 yr (the Nyquist period for the 1 yr sampling of our inverted model coefficients). In practice we use a Butterworth filter of order 2. The fit of (7) to the correlation for the filtered RC (using the *curve_fit* python function based on Vugrin et al, 2007) gives the following values, $\sigma_1^2 = 64.9 \text{ nT}^2$, $\sigma_2^2 = 23.1 \text{ nT}^2$, $1/\alpha_1 = 2.6 \text{ yr}$, $1/\alpha_2 = 23.6 \text{ yr}$, and $2\pi/\omega_2 = 11.7 \text{ yr}$, that we approximate to the values given in Table 1. The period $2\pi/\omega_2$ of the damped oscillator is reminiscent of the solar cycle. The amplitude of the AR-1 process is larger by a factor ≈ 1.6 than that of the AR-2 process. The fit to the RC correlation function is shown on Fig. 4.

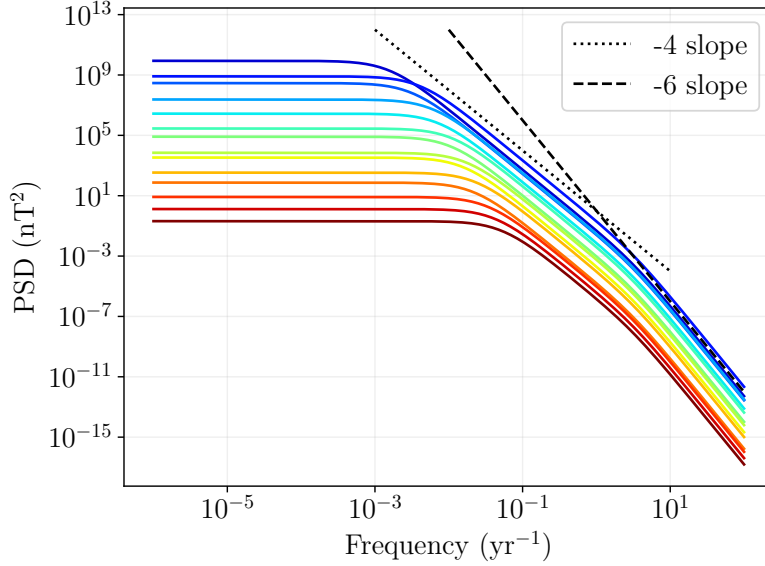


Figure 3: PSD associated with the COV-OBS.x3 model a priori cross-correlation function considered for all coefficients but the axial dipole. The color indicates the coefficient degree, where blue is associated with the lowest degrees (starting at $l = 1$) and red the highest ones (up to $l = 14$).

σ_2^2 (nT ²)	$1/\alpha_2$ (years)	$2\pi/\omega_2$ (years)	σ_1^2 (nT ²)	$1/\alpha_1$ (years)
25	25	11.5	65	2.5

Table 1: Parameters for the correlation function (7) used as a prior on \tilde{q}_1^0 in the construction of COV-OBS.x3 .

3.3 Inversion procedure

As for previous editions of the COV-OBS models, COV-OBS.x3 Gauss coefficients have been inverted with a Newton-Raphson algorithm. One evolution w.r.t. earlier releases is the consideration of Huber weights for the measure of the residuals (data misfit) instead of a L_2 norm previously. This avoids the use of a strict rejection criterion (previously 3σ , now at 10σ), and we now rely on an iterative weighted least-square method (Farquharson and Oldenburg, 1998). The use of the Huber norm is a common way for dealing with outliers.

Model coefficients for all epochs and all degrees are stored into a vector \mathbf{m} , of size $P = N(L(L + 2) + 1) = 5850$. Our inversion problem thus leads to minimize a functional sum of:

- The misfit to the data

$$\mathcal{M}_y = \sum_{i=1}^{N^o} \mathcal{L}_c(\epsilon_i), \text{ with } \epsilon_i = |y_i - H_i(\mathbf{m})|/\sigma_i. \quad (8)$$

H_i is the forward operator for the i -th datum y_i , associated with uncertainties σ_i . N^o is the total number of observations. \mathcal{L}_c is the Huber loss function defined as (e.g. Olsen, 2002)

$$\mathcal{L}_c(\epsilon) = \begin{cases} \epsilon^2/2 & |\epsilon| \leq c \\ c|\epsilon| - c^2/2 & \text{otherwise} \end{cases}, \quad (9)$$

with $c = 1.5$ the parameter controlling the normalized residual value above which the measure

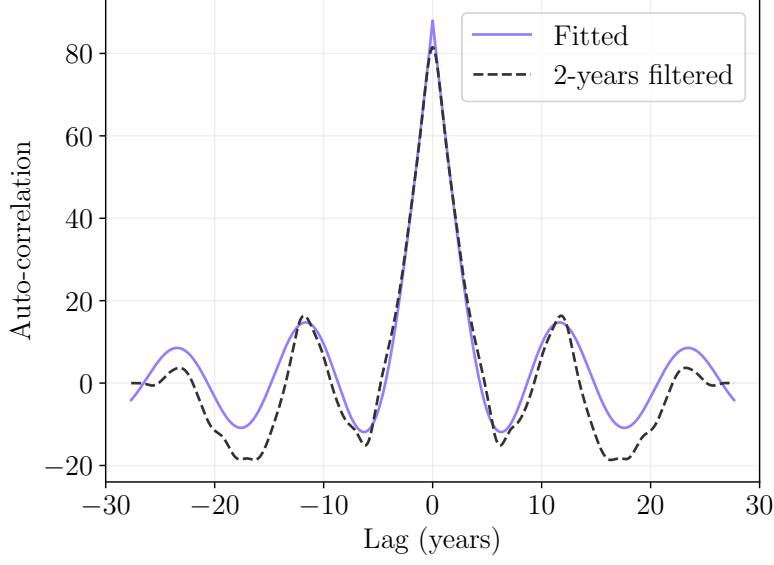


Figure 4: Cross-correlation function for the external dipole coefficient \tilde{q}_1^0 , as inferred from the RC index lowpass filtered for periods longer than 2 yr (see text for details).

morph from a $L2$ measure (for low $|\epsilon|$) to a $L1$ measure. Observation errors are supposed independent.

- A measure of the model complexity

$$\mathcal{N}_m = (\mathbf{m} - \mathbf{m}^b)^T \mathbf{P}^{-1} (\mathbf{m} - \mathbf{m}^b) . \quad (10)$$

The matrix \mathbf{P} contains, for all coefficients, the temporal cross-covariance between all epochs, as described in §3.2.1-3.2.2. We assume a priori that the coefficients of different orders or degrees are independent. \mathbf{m}^b is the background model. It is 0 for all coefficients but the axial dipole $g_1^{0b} = -24000$ nT (from paleomagnetic reconstructions) and the external dipole $\tilde{q}_1^{0b} = -20$ nT (the same values used for COV-OBS.x2).

The iterative process is stopped after 10 iterations, after which the relative change in the SV norm at the CMB averaged over the full era, from one iteration to the next, is less than 10^{-3} . Note that the projection onto wide correlation functions (instead of B-splines) comes with a numerical cost, as the filling of the matrices does not rely anymore on a banded storage.

3.4 Interpolating and forecasting Gauss coefficients

Gauss coefficients are interpolated and forecasted based on the correlation functions, within a Gaussian regression framework (Rasmussen and Williams, 2006). We follow the approach of Hellio and Gillet (2018), considering each coefficient individually. We store in a vector \mathbf{g}_x its values to be interpolated and/or extrapolated at a set of epochs \mathbf{t}_x , and in a vector \mathbf{g}_m its inverted values at the set of epochs \mathbf{t}_m considered above to build the field model. Based on the cross-covariance functions defined above, we build the cross-covariance matrices $\mathbf{P}_{mm} = \mathbb{E}(\mathbf{g}_m \mathbf{g}_m^T)$, $\mathbf{P}_{xx} = \mathbb{E}(\mathbf{g}_x \mathbf{g}_x^T)$ and $\mathbf{P}_{xm} = \mathbb{E}(\mathbf{g}_x \mathbf{g}_m^T)$ for all pairs of epochs within \mathbf{t}_x and \mathbf{t}_m . Under Gaussian assumptions for the model distribution and uncertainties, the most likely estimate at epochs \mathbf{t}_x is then

$$\mathbf{g}_x = \mathbf{g}_m^b + \mathbf{P}_{xm} [\mathbf{P}_{mm} + \mathbf{R}]^{-1} (\mathbf{g}_m - \mathbf{g}_m^b) , \quad (11)$$

where \mathbf{R} is the cross-covariance error matrix on the model parameters \mathbf{g}_m , and \mathbf{g}_m^b is fed with the background model coefficients. Eq. (11) is used to calculate the model predictions at any data epoch t_i , when building the operator $H_i(\mathbf{m})$ entering the cost function. In this case we consider within the iterative process $\mathbf{R} = 0$. The same Eq. (11) is used to provide our model estimates and its associated uncertainties at any epochs, both for interpolating and for forecasting. In this case \mathbf{R} is built from diagonal elements of the posterior model cross-covariance matrix (the inverse of the Hessian), as operated by Gillet et al (2013). This simple approach (separately for each coefficient) avoids manipulating too large cross-covariance matrices (reducing numerical instabilities associated with too wide ranges of eigenvalues).

On top of this estimate for the model coefficient series \mathbf{g}_x at epochs \mathbf{t}_x , we also provide the associated uncertainties based on the posterior model error covariance matrix

$$\mathbf{P}_{xx}^{\text{post}} = \mathbf{P}_{xx} - \mathbf{P}_{xm} [\mathbf{P}_{mm} + \mathbf{R}]^{-1} \mathbf{P}_{xm}^T. \quad (12)$$

In order to derive numerical values of the uncertainties on \mathbf{g}_x , we first perform the Cholesky factorization $\mathbf{P}_{xx}^{\text{post}} = \mathbf{L}\mathbf{L}^T$. From the the lower triangle matrix \mathbf{L} we then generate an ensemble of $N^e = 500$ realizations

$$\mathbf{g}_{x,i} = \mathbf{L}\mathbf{w}_i \text{ for } i \in [1, N^e], \quad (13)$$

where \mathbf{w}_i is a centered and unit variance normal random vector. The dispersion within this ensemble of series gives us a hint of the model uncertainties through time.

4 Results and IGRF candidate models

4.1 Misfits and predictions to GO and GVO series

We provide in Table 2 some statistics stemming from COV-OBS.x3 predictions to the GO SV and GVO MF data. These are produced separately for all components and for all satellite missions. The diagnostics are provided for the X (Northward), Y (Eastward), Z (downward) components of the field, as well as for its intensity F . We introduce for each subset of data the dimensional and adimensional measures of the misfits and biases. To this purpose we fit a Huber distribution (see Eq. 9)

$$p_c(\epsilon) = \frac{1}{\sqrt{2\pi}\chi^{\star 2}} \exp\left(-\mathcal{L}_c\left(\frac{\epsilon - \mu^{\star}}{\chi^{\star}}\right)\right) \quad (14)$$

to the normalized histograms of the dimensionless residuals ϵ , with the dimensionless bias μ^{\star} and misfit χ^{\star} being the two adjustable parameters. The dimensional diagnostics are obtained similarly from histograms of the dimensional residuals, by adjusting here three parameters: a dimensional bias μ and misfit χ , as well as the parameter c . The adjusted misfit values are given in Table 2 (for "core" field data) and 3 (for "observed" minus "core" field data). Fitted values of the biases and c are given in Appendix C.

For "core" data, apart from Oersted (X and F), Grace (X) and CryoSat (Z and F) data, dimensionless biases are less than 0.1 in absolute value. For all components, GO as well as CHAMP and Swarm data, that bring the most important observational constraint, show almost centered distributions for normalized residuals. Dimensionless residuals are generally less than unity, denoting a possible over-estimation of the a priori data uncertainties, in particular for CHAMP and Swarm. The lower dimensional misfits are found for CHAMP and Swarm, where it is less than 1 nT for X, Y and F , and only slightly above 1 nT for Z data. All components from GO and CryoSat data are fitted within 1.7 nT. Unsurprisingly, the larger misfits values are found for Oersted and Grace GVO data. The fitted parameter c for dimensional misfits ranges from 1.2 and 1.8 nT, in reasonable agreement with the observed misfits.

Dataset	N^o				χ^*				χ (nT)			
	X	Y	Z	F	X	Y	Z	F	X	Y	Z	F
GO	8982	9014	9040	0	0.97	0.63	0.51	–	1.44	1.35	1.68	–
CH	2366	2368	2368	436	0.36	0.43	0.5	0.29	0.75	0.87	1.03	0.85
CR	2024	2026	2026	440	0.57	0.55	0.8	0.53	1.32	1.21	1.62	1.47
GR	2279	2283	2284	490	0.64	0.75	0.74	0.33	1.61	1.9	1.95	1.19
SW	7316	7331	7333	1501	0.45	0.37	0.55	0.3	0.89	0.83	1.04	0.86
OR	1076	1077	1078	222	1.04	0.73	0.71	0.49	2.13	1.8	1.69	1.65

Table 2: Number of data and prediction errors statistics for GO SV data and GVO ("core") MF data used when fitting the COV-OBS.x3 model. See text for details. All dimensional values are given in nT (resp. nT/yr) for the MF (resp. SV) data.

Dimensional misfits for "observed" minus "core" field data, used to estimate our external field model, show relatively larger values, ranging from 2 to 4.5 nT depending on the mission and components. The distinction between the several missions is less obvious than for "core" field data, whose quality is leveled by the crude external model considered in this study. Still normalized misfits are less than unity, in particular for the less accurate Oersted, CryoSat and Grace data, suggesting that a priori error uncertainties considered in our inverse problem are possibly over-estimated. We note also for all satellite missions significant biases for F data (and to a lesser extent on X too). The fitted parameter c for dimensional misfits are larger than for "core" field data, ranging from 1.0 and 2.5 nT, in reasonable agreement with the observed misfits.

Dataset	N^o				χ^*				χ (nT)			
	X	Y	Z	F	X	Y	Z	F	X	Y	Z	F
CH	2366	2368	2368	436	0.95	0.53	0.75	0.62	3.41	2.19	3.04	2.74
CR	2024	2026	2026	440	0.48	0.41	0.37	0.37	2.88	2.55	2.43	2.43
GR	2279	2283	2284	490	0.31	0.42	0.3	0.18	2.97	4.29	3.13	2.03
SW	7316	7331	7333	1501	1.43	0.62	0.83	0.88	3.92	2.13	2.55	3.18
OR	1076	1077	1078	222	0.7	0.39	0.4	0.53	3.07	2.24	2.75	3.03

Table 3: Same as Table 2 for GVO ("observed" minus "core") MF data, associated with our external field model.

In addition, we represent on Fig. 5 for all missions and components the distribution of normalized residuals ϵ , superimposed with the best fitting Huber distribution. Most histograms behave according to our assumptions on the residuals distribution. In some cases the PDF behaves closer to a Laplacian (e.g. for the X component for CHAMP and SWARM), with a sharper peak around 0. Likewise, some asymmetries are seen for some PDF for F data.

Further illustration of our model ability to fit observations is depicted on Fig. 6 with SV series at the Honolulu and Hermanus ground stations, and on Fig. 7 with MF series at two nearby GVO positions. Our model closely fits the observed series, with predictions comparable to those from CHAOS-7.

4.2 Time evolution of field model coefficients

We now illustrate on Fig. 8 the evolution of some SV coefficients inferred from COV-OBS.x3, in comparison with alternative models CHAOS-7, KALMAG and COV-OBS.x2. The estimation is operated with every 0.2 yr over the period, using the method described in §3.4.

We note some significant changes in the rapid evolution of the axial dipole between COV-OBS.x3 and COV-OBS.x2. Our new model is closer to CHAOS-7, and generally to KALMAG (to the exception of the period from 2010 to 2014 where CHAOS-7 and KALMAG differ the most). This is in part due to our revised parameterization of the external field (for which we now neglect induction in the

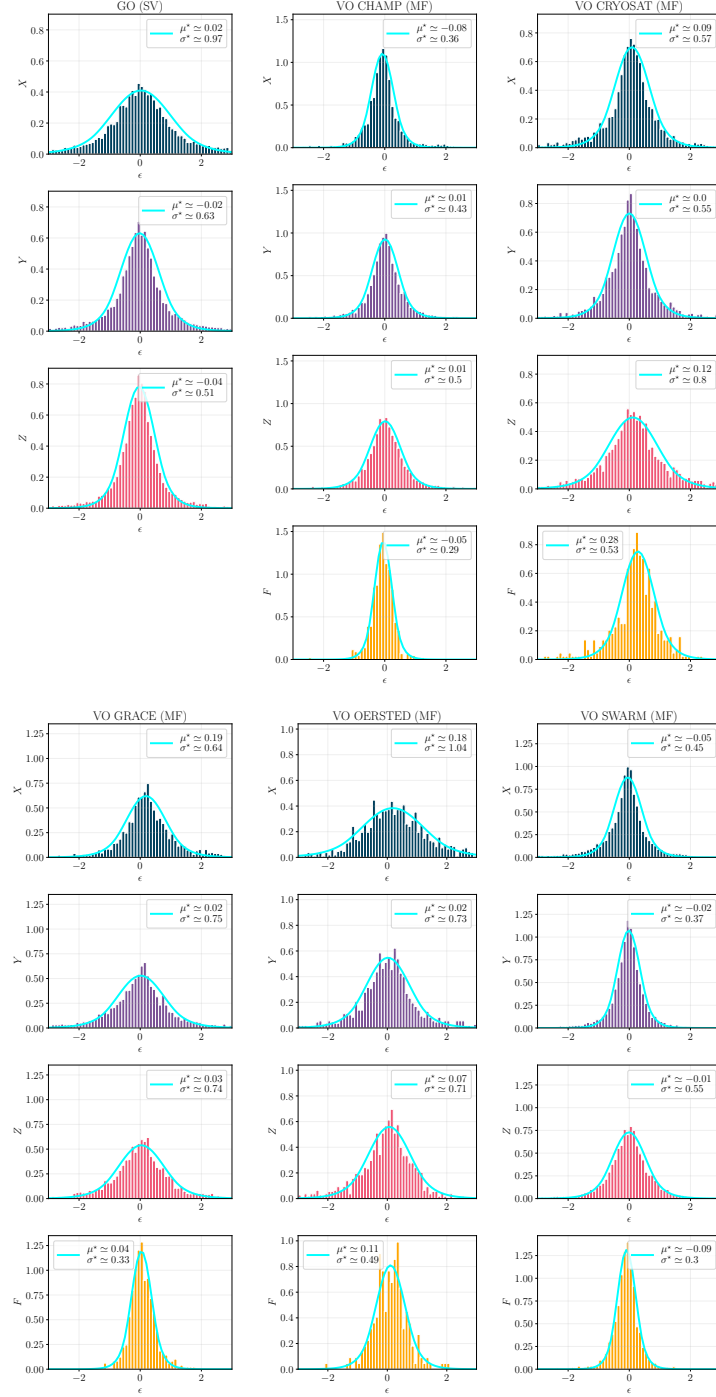


Figure 5: Histogram of the normalized misfits ϵ for the various GO and GVO datasets, splitted into spatial components. The cyan curve represents the Huber distribution associated with the normalized misfits.

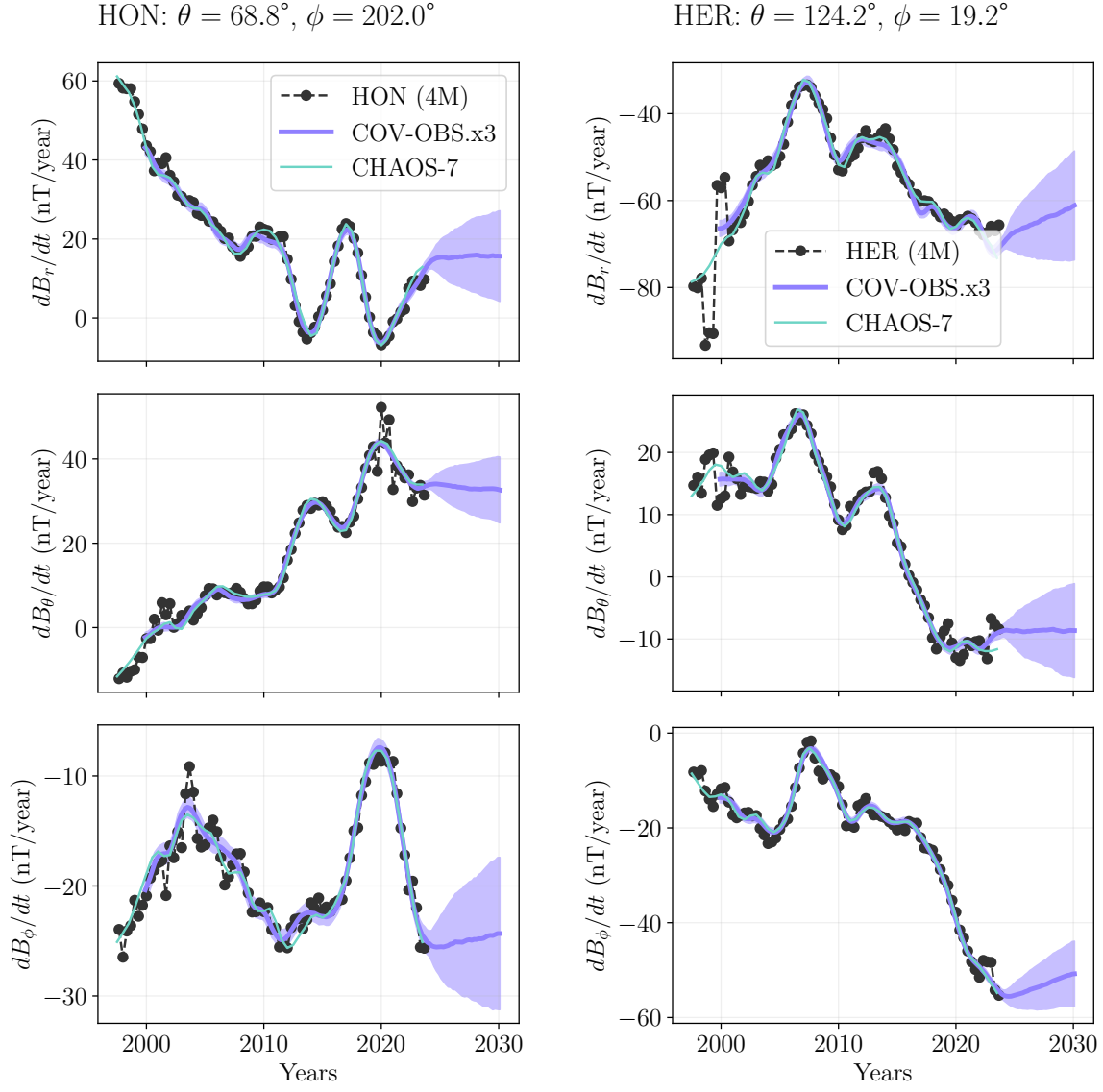


Figure 6: Comparison between the SV observed at Honolulu (HON) and Hermanus (HER), and the predictions from COV-OBS.x3 and CHAOS-7, for the three components. Shaded areas represents the spread within $\pm 1\sigma$.

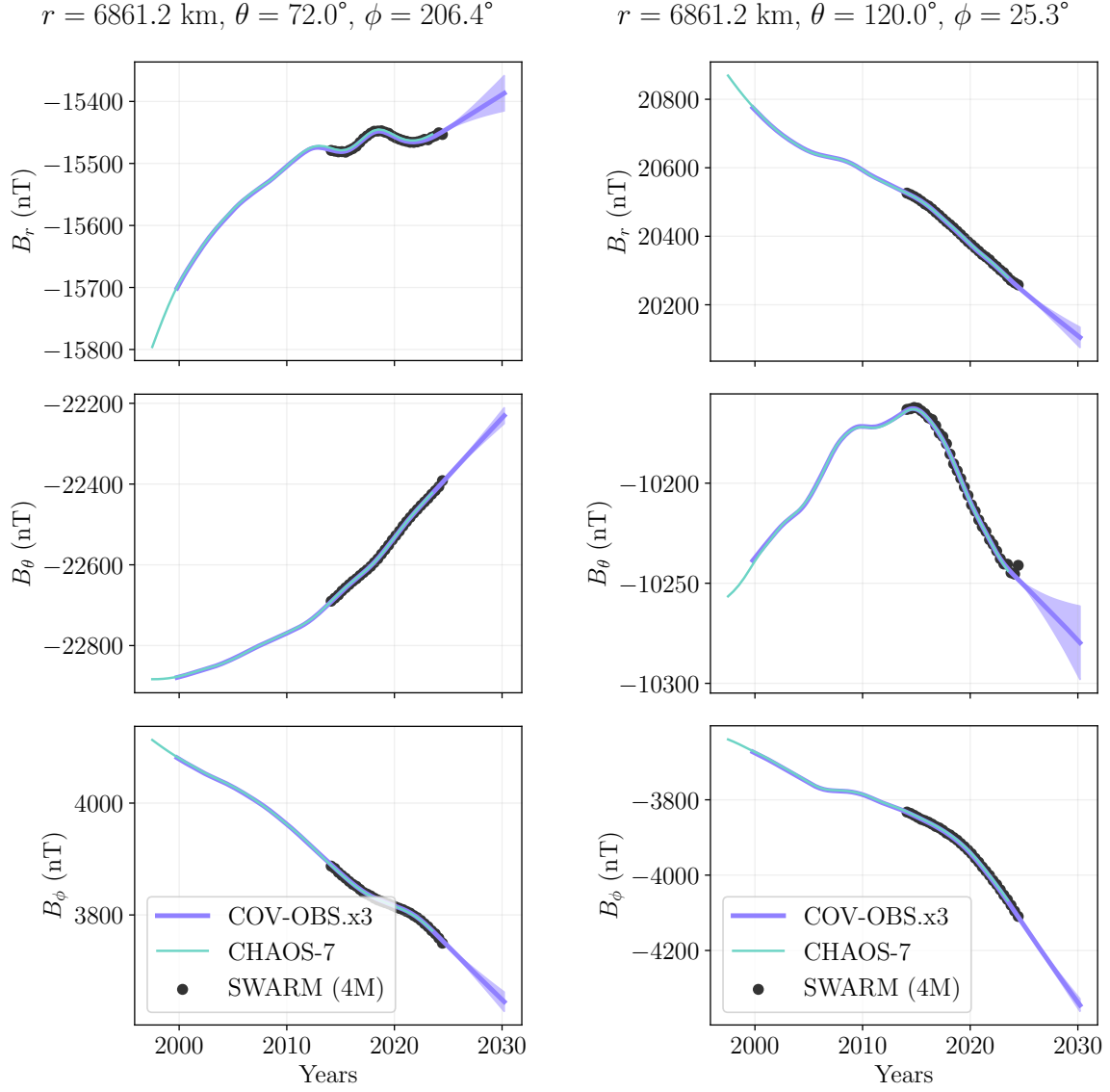


Figure 7: Comparison between the MF observed at two GVO and the predictions from COV-OBS.x3 and CHAOS-7, for the three components. Shaded areas represents the spread within $\pm 1\sigma$.

core, see above) and to our new approach at constraining the external field from differences between "core" and "observed" MF GVO series (instead of a co-estimation from alternative GVO uncleaned for magnetospheric sources as in COV-OBS.x2). For other coefficients at low to moderate degrees l , the series overlap between the several considered models.

Interestingly, our estimate of the model uncertainties is larger in comparison with our previous COV-OBS release, for all coefficients including the axial dipole. This is partly the consequence of dropping out the projection onto splines with 2 yr knot spacing. This latter was indeed leading to an estimate of errors on a low-pass filtered vision of the Gauss coefficients, typically for periods longer than 3–4 years. Our error estimate is larger than that from KALMAG on short length-scale coefficients.

Furthermore, we observe that the spread of the SV forecast behaves smoothly once the observational constraint is relaxed after $t_e = 2024.5$. This is characteristic of AR-3 processes considered in this study, for which the SV is continuous and differentiable, with a spread evolving $\propto (t - t_e)^{3/2}$. It contrasts with AR-2 processes for which the SV is only continuous, translating in a spread sharply increasing ($\propto \sqrt{t - t_e}$), as observed for instance for the KALMAG model on Fig. 8.

Finally we present on Fig. 9 the evolution of the external field coefficients \tilde{g}_1^0 . It overall exhibits variations similar to those from COV-OBS.x2, although showing slightly more rapid variations. It is relatively close to the RC index once low-pass filtered for periods longer than 2 years (using a Butterworth filter of order 2), meaning that our estimate is a decent approximation for the slow evolution of the magnetospheric ring current.

4.3 Extracting the DGRF and IGRF candidates model coefficients

We derive the coefficients of our candidate models from our above estimate, generating an ensemble of model series over 2000–2030. The DGRF MF coefficients in 2020 are then estimated as

$$\mathbf{g}_{\text{DGRF}} = \langle \mathbf{g}(2020) \rangle, \quad (15)$$

where $\langle \dots \rangle$ denote the ensemble average. Similarly the IGRF MF coefficients in 2025 are given by

$$\mathbf{g}_{\text{IGRF}} = \langle \mathbf{g}(2025) \rangle, \quad (16)$$

and the average SV over 2025–2030 by

$$\dot{\mathbf{g}}_{\text{IGRF}} = \frac{1}{2030 - 2025} \int_{2025}^{2030} \langle \dot{\mathbf{g}} \rangle(t) dt = \frac{\langle \mathbf{g}(2030) \rangle - \langle \mathbf{g}(2025) \rangle}{2030 - 2025}. \quad (17)$$

Associated uncertainties are estimated from the dispersion within the ensemble of models, as

$$\delta \mathbf{g}_{\text{IGRF}} = \sqrt{\frac{1}{N^e} \sum_{i=1}^{N^e} (\mathbf{g}_i(2025) - \mathbf{g}_{\text{IGRF}})^2}, \quad (18)$$

with a similar definition for $\delta \mathbf{g}_{\text{DGRF}}$ in 2020. Uncertainties on the 5 yr SV prediction is given by

$$\delta \dot{\mathbf{g}}_{\text{IGRF}} = \sqrt{\frac{1}{N^e} \sum_{i=1}^{N^e} \left(\frac{\mathbf{g}_i(2030) - \mathbf{g}_i(2025)}{2030 - 2025} - \dot{\mathbf{g}}_{\text{IGRF}} \right)^2}. \quad (19)$$

For those three products, maps of the radial components at the Earth's surface and at the core surface are shown on Fig. 10

Acknowledgements

We thank ESA for the prompt availability of *Swarm* L1b data and for providing access to the CryoSat-2 platform magnetometer data and related engineering information. The support of the CHAMP mission by the German Aerospace Center (DLR) and the Federal Ministry of Education and Research for

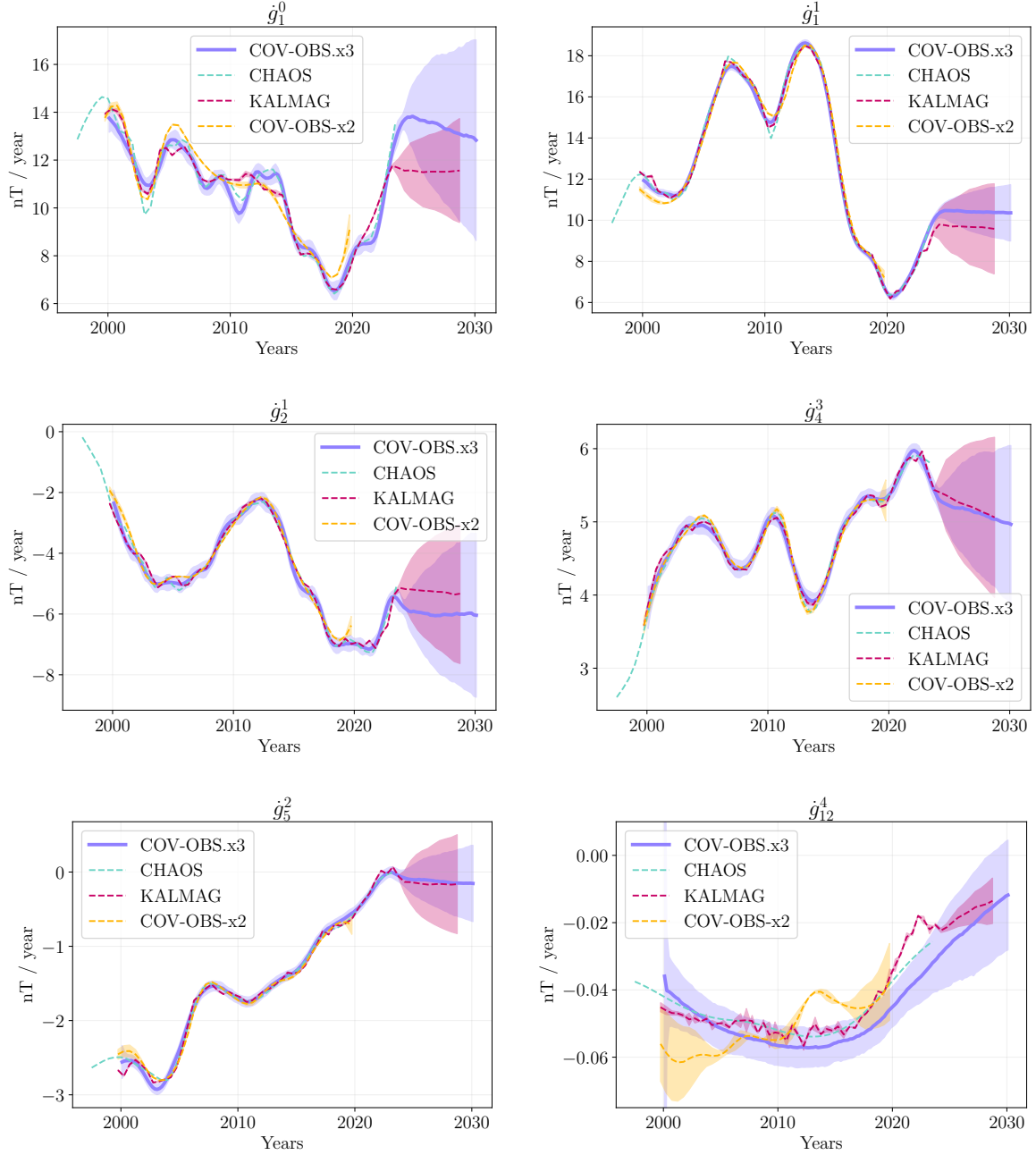


Figure 8: SV time series for several Gauss coefficients COV-OBS.x3, compared with COV-OBS.x2, CHAOS and KALMAG. For models provided with uncertainties, shaded areas represent the spread within $\pm 1\sigma$.

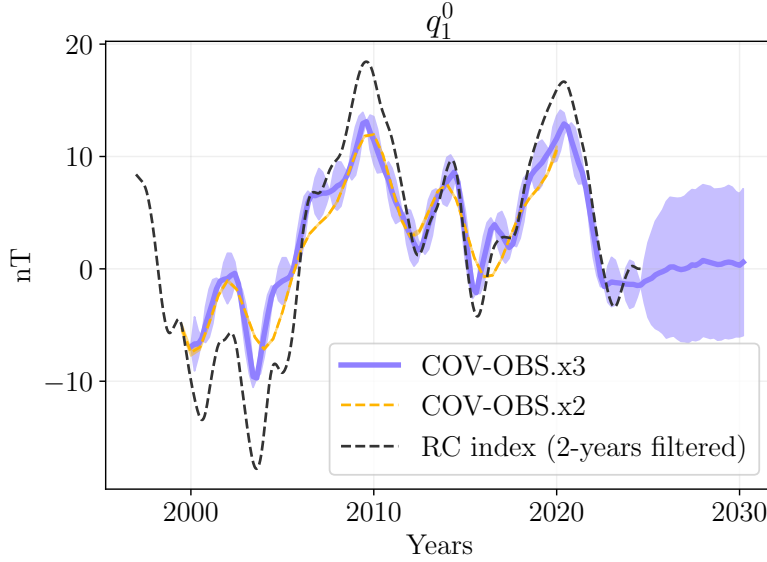


Figure 9: Time evolution of the external field coefficient \tilde{q}_1^0 for COV-OBS.x3, compared with its predecessor COV-OBS.x2 and the RC index low-pass filtered for periods longer than 2 years. Shaded areas represent the spread within $\pm 1\sigma$.

the CHAMP mission is gratefully acknowledged. The Ørsted Project was made possible by extensive support from the Danish Government, NASA, ESA, CNES, DARA and the Thomas B. Thrige Foundation. The staff of the geomagnetic observatories and INTERMAGNET are thanked for supplying high-quality observatory data. This work has been funded by ESA in the framework of EO Science for Society, through contract 4000127193/19/NL/IA (Swarm + 4D Deep Earth: Core). It was also partially supported by the CNES. RC and NG are part of Labex OSUG@2020 (ANR10 LABX56).

References

- Alken P, Thébaud E, Beggan CD, Amit H, Aubert J, Baerenzung J, Bondar T, Brown W, Califf S, Chambodut A, et al (2021) International geomagnetic reference field: The thirteenth generation. *Earth, Planets and Space* 73:1–25
- Aubert J, Gillet N (2021) The interplay of fast waves and slow convection in geodynamo simulations nearing Earth’s core conditions. *Geophys J Int* 225(3):1854–1873
- Baerenzung J, Holschneider M, Saynisch-Wagner J, Maik T (2022) Kalmag: a high spatio-temporal model of the geomagnetic field. *Earth, Planets and Space* 74(1):139
- Barrois O, Hammer MD, Finlay CC, Martin Y, Gillet N (2018) Assimilation of ground and satellite magnetic measurements: inference of core surface magnetic and velocity field changes. *Geophys J Int* 215(1):695–712
- Bloxham J, Jackson A (1992) Time-dependent mapping of the magnetic field at the core-mantle boundary. *J Geophys Res: Solid Earth* 97(B13):19,537–19,563
- Bouligand C, Gillet N, Jault D, Schaeffer N, Fournier A, Aubert J (2016) Frequency spectrum of the geomagnetic field harmonic coefficients from dynamo simulations. *Geophys J Int* 207(2):1142–1157

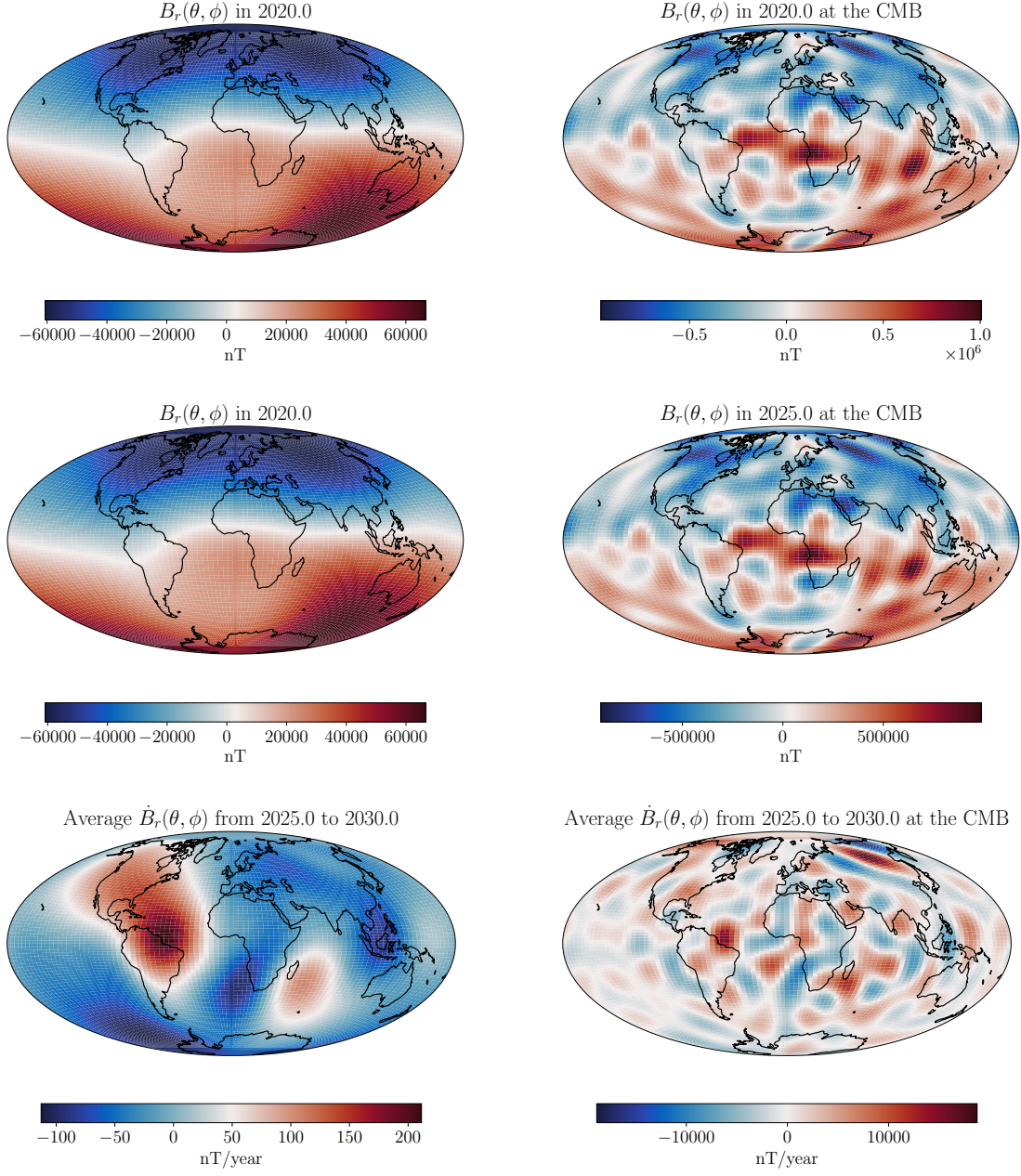


Figure 10: Maps of the radial component for the MF in 2020 (top), in 2025 (middle) and for the time-average SV over 2025–2030 (bottom). At the Earth's surface (left) and at the core surface (bottom).

- Buffett B, Puranam A (2017) Constructing stochastic models for dipole fluctuations from paleomagnetic observations. *PhysEarth Planet Int* 272:68–77
- Constable C, Johnson C (2005) A paleomagnetic power spectrum. *PhysEarth Planet Int* 153(1-3):61–73
- Farquharson CG, Oldenburg DW (1998) Non-linear inversion using general measures of data misfit and model structure. *Geophys J Int* 134(1):213–227, DOI 10.1046/j.1365-246x.1998.00555.x
- Finlay C, Lesur V, Thébault E, Vervelidou F, Morschhauser A, Shore R (2017) Challenges handling magnetospheric and ionospheric signals in internal geomagnetic field modelling. *Space Science Reviews* 206(1):157–189
- Finlay C, Kloss C, Olsen N, Hammer M, Tøffner-Clausen L, Grayver A, Kuvshinov A (2020) The CHAOS-7 geomagnetic field model and observed changes in the South Atlantic Anomaly. *Earth Planets Space* 72(1):1–31
- Gillet N, Jault D, Canet E, Fournier A (2010) Fast torsional waves and strong magnetic field within the Earth’s core. *Nature* 465(7294):74–77
- Gillet N, Jault D, Finlay C, Olsen N (2013) Stochastic modeling of the earth’s magnetic field: Inversion for covariances over the observatory era. *Geochemistry, Geophysics, Geosystems* 14(4):766–786
- Gillet N, Barrois O, Finlay CC (2015) Stochastic forecasting of the geomagnetic field from the cov-obs.x1 geomagnetic field model, and candidate models for igrf-12. *Earth, Planets and Space* 67:1–14
- Hammer MD, Cox GA, Brown WJ, Beggan CD, Finlay CC (2021) Geomagnetic virtual observatories: monitoring geomagnetic secular variation with the swarm satellites. *Earth Planets Space* 73(1):1–22
- Hellio G, Gillet N (2018) Time-correlation-based regression of the geomagnetic field from archeological and sediment records. *Geophys J Int* 214(3):1585–1607
- Huder L, Gillet N, Finlay CC, Hammer MD, Tchoungui H (2020) COV-OBS.x2: 180 years of geomagnetic field evolution from ground-based and satellite observations. *Earth, Planets and Space* 72(1):160
- Hulot G, Le Mouél J (1994) A statistical approach to the earth’s main magnetic field. *Phys Earth Planet Int* 82(3-4):167–183
- Kloss C, Finlay CC, Olsen N (2021) Co-estimating geomagnetic field and calibration parameters: modeling earth’s magnetic field with platform magnetometer data. *Earth, Planets and Space* 73:1–21
- Lesur V, Wardinski I, Baerenzung J, Holschneider M (2018) On the frequency spectra of the core magnetic field gauss coefficients. *Phys Earth Planet Int* 276:145–158
- Lesur V, Gillet N, Hammer M, Mandea M (2022) Rapid variations of Earth’s core magnetic field. *Surv Geophys* pp 1–29
- Lhuillier F, Fournier A, Hulot G, Aubert J (2011) The geomagnetic secular-variation timescale in observations and numerical dynamo models. *Geophys Res Lett* 38(9)
- Macmillan S, Olsen N (2013) Observatory data and the swarm mission. *Earth, Planets and Space* 65:1355–1362
- Morzfeld M, Buffett BA (2019) A comprehensive model for the kyr and myr timescales of earth’s axial magnetic dipole field. *Nonlinear Processes in Geophysics* 26(3):123–142
- Olsen N (2002) A model of the geomagnetic field and its secular variation for epoch 2000 estimated from ørsted data. *Geophys J Int* 149(2):454–462

- Olsen N, Lühr H, Finlay CC, Sabaka TJ, Michaelis I, Rauberg J, Tøffner-Clausen L (2014) The CHAOS-4 geomagnetic field model. *Geophys J Int* 197(2):815–827
- Rasmussen CE, Williams C (2006) *Gaussian processes for machine learning* the mit press. Cambridge, MA 32:68
- Sabaka TJ, Olsen N, Purucker ME (2004) Extending comprehensive models of the earth’s magnetic field with ørsted and champ data. *Geophys J Int* 159(2):521–547
- Sabaka TJ, Tøffner-Clausen L, Olsen N, Finlay CC (2018) A comprehensive model of earth’s magnetic field determined from 4 years of swarm satellite observations. *Earth, Planets and Space* 70:1–26
- Vugrin KW, Swiler LP, Roberts RM, Stucky-Mack NJ, Sullivan SP (2007) Confidence region estimation techniques for nonlinear regression in groundwater flow: Three case studies. *Water Resources Research* 43(3)
- Yaglom AM (2004) *An introduction to the theory of stationary random functions*. Courier Corporation

A From the PSD to the correlation function

We derive here an AR-3 correlation function that satisfies the observational and numerical constraints from §3.2. Below we rely on the properties of AR-1 processes with variance σ_0^2 and decay frequency ω_0 , which are characterized by a cross-covariance function

$$C(\tau) = \sigma_0^2 \exp(-\omega_0|\tau|) \quad (20)$$

and a PSD (e.g. Yaglom, 2004)

$$S(\omega) = \frac{\sigma_0^2 \omega_0 / \pi}{\omega_0^2 + \omega^2} . \quad (21)$$

First we perform a decomposition in simple fractions of a PSD of the form (6). Consider three constants (a, b, c) , and three frequencies (α, β, γ) . Lets choose a PSD such that

$$\begin{aligned} S(\omega) &= \frac{1}{\pi} \left(\frac{a\alpha}{\alpha^2 + \omega^2} + \frac{b\beta}{\beta^2 + \omega^2} + \frac{c\gamma}{\gamma^2 + \omega^2} \right) \\ &= \frac{k_0 + k_2\omega^2 + k_4\omega^4}{(\alpha^2 + \omega^2)(\beta^2 + \omega^2)(\gamma^2 + \omega^2)} , \end{aligned} \quad (22)$$

where

$$\begin{cases} \pi k_4 = a\alpha + b\beta + c\gamma \\ \pi k_2 = a\alpha(\beta^2 + \gamma^2) + b\beta(\alpha^2 + \gamma^2) + c\gamma(\alpha^2 + \beta^2) \\ \pi k_0 = a\alpha\beta^2\gamma^2 + b\beta\alpha^2\gamma^2 + c\gamma\alpha^2\beta^2 \end{cases} \quad (23)$$

Using Eq. (20,21), the correlation function associated with the PSD (22) takes the simple form

$$C(\tau) = a \exp(-\alpha|\tau|) + b \exp(-\beta|\tau|) + c \exp(-\gamma|\tau|) . \quad (24)$$

For $S(\omega)$ to evolve as ω^{-6} towards high frequencies, we deduce the two conditions $k_2 = k_4 = 0$. Imposing the variance $\sigma^2 = C(0)$ of the signal leads to a third condition $\sigma^2 = a + b + c$. Knowing

the values for the three frequencies (α, β, γ) and σ^2 , we then have to solve the linear problem $\mathbf{M}\mathbf{x} = \mathbf{y}$ where

$$\mathbf{M} = \begin{bmatrix} 1 & 1 & 1 \\ \alpha & \beta & \gamma \\ \alpha(\beta^2 + \gamma^2) & \beta(\alpha^2 + \gamma^2) & \gamma(\alpha^2 + \beta^2) \end{bmatrix}, \quad (25)$$

$$\mathbf{x} = \begin{bmatrix} a \\ b \\ c \end{bmatrix} \quad \text{and} \quad \mathbf{y} = \begin{bmatrix} \sigma^2 \\ 0 \\ 0 \end{bmatrix}.$$

We have

$$\det(\mathbf{M}) = \gamma\beta(\beta^2 - \gamma^2) - \alpha\gamma(\alpha^2 - \gamma^2) + \alpha\beta(\alpha^2 - \beta^2), \quad (26)$$

and the solution is

$$\begin{cases} a/\sigma^2 = \frac{\gamma\beta(\beta^2 - \gamma^2)}{\det(M)} \\ b/\sigma^2 = \frac{-\alpha\gamma(\alpha^2 - \gamma^2)}{\det(M)} \\ c/\sigma^2 = \frac{\alpha\beta(\alpha^2 - \beta^2)}{\det(M)} \end{cases}. \quad (27)$$

From these values we deduce the cross-covariance functions (24), that we use to build the prior covariance matrix when building our field model.

For all coefficients but the axial dipole, we could resort to only 3 spectral ranges of indices $p = 0, -4$ and -6 . However we cannot use $T_u = T_d$ ($\beta = \alpha$), since in this case $c = 0$ and then the PSD will behave as ω^{-4} on short time-scales. However, this pathological case can be avoided by having α close to β , a bit larger.

The PSD and cross-covariance functions obtained this way are characteristic of the AR-3 process represented as

$$X''' + (\alpha + \beta + \gamma) X'' + (\alpha\beta + \beta\gamma + \gamma\alpha) X' + \alpha\beta\gamma X = Z, \quad (28)$$

where Z is a centered white noise of variance

$$k_0 = \frac{\alpha\beta\gamma\sigma^2}{\pi\det(\mathbf{M})} (\beta^2\gamma^2(\beta^2 - \gamma^2) - \alpha^2\gamma^2(\alpha^2 - \gamma^2) + \alpha^2\beta^2(\alpha^2 - \beta^2)). \quad (29)$$

For the parameters chosen here, the roots of the denominator of (22) being complex conjugates, a process such as (28) is stationary. Note that we may simplify Eq. (27) in the limit $\gamma \gg \beta \gg \alpha$ (as for the axial dipole), in which case $\det(\mathbf{M}) \simeq -\beta\gamma^3$, leading to

$$\begin{cases} a/\sigma^2 \simeq 1 \\ b/\sigma^2 \simeq -\frac{\alpha}{\beta} \\ c/\sigma^2 \simeq \frac{\alpha\beta^2}{\gamma^3} \end{cases}. \quad (30)$$

Then one has $k_0 \simeq \sigma^2\alpha\beta^2\gamma^2/\pi$.

B Choice of the input parameters

The AR-3 correlation functions designed above rely on the choice of some parameters. We consider here $\alpha^{AD} = \omega_d = 10^{-4} \text{ yr}^{-1}$ for the axial dipole. We also fix $\gamma = \omega_a = 2\pi/T_a = \pi \text{ yr}^{-1}$ for all coefficients.

We now wish to choose the frequency $\beta(n) = \omega_u$. We define $\omega_u(n)$ as performed for previous COV-OBS models, i.e. based on the SV time-scale (5). The reason is that $\tau_{SV}(n)$ is a quantity accessible from geophysical observations via magnetic field models. To this purpose we use the relationship (e.g. Hulot and Le Mouél, 1994)

$$\mathbb{E}(\dot{X}^2) = -\frac{d^2 C(\tau)}{d\tau^2} \Big|_{\tau=0}, \quad (31)$$

for a process $X(t)$ with auto-covariance function $C(\tau)$. For a function such as that defined by Eq. (24), we then have

$$\sigma_{\dot{g}_n^m}^2 = -(a\alpha^2 + b\beta^2 + c\gamma^2). \quad (32)$$

Using (27) in the limit where $\gamma \gg \alpha, \beta$ we get

$$\alpha\beta(n) = 1/\tau_{SV}^2(n). \quad (33)$$

For all coefficients but the axial dipole, if we assume as above the condition $c\alpha = \beta$ with c a bit larger than one (to reduce the frequency range presenting a -2 spectral index), this gives

$$\beta(n) = c\alpha(n) = \omega_u(n) = \frac{\sqrt{c}}{\tau_{SV}(n)}. \quad (34)$$

This condition is close to that introduced previously by Gillet et al (2013) for the cut-off frequency of Matern AR-2 processes. For the axial dipole (noted with a subscript ‘AD’) we obtain instead

$$\omega_d\beta^{AD} = 1/\tau_{SV}^{AD^2}, \quad (35)$$

where $\tau_{SV}^{AD} = \sqrt{\sigma_{g_1^0}^2/\sigma_{g_1^0}^2}$. A numerical application with $1/\omega_d = 10^4$ yr, $\sigma_{\dot{g}_1^0} = 10$ nT/yr and $\sigma_{g_1^0} = 7700$ nT (or $\tau_{SV}^{AD} = 7700$ yr, see Huder et al, 2020) leads to $1/\beta^{AD} \approx 60$ yr $\gg T_a$. We check a posteriori that $\omega_d \ll \beta^{AD} \ll \omega_a$.

C Additional statistics

C.1 For the internal field

Dataset	μ^*				μ (nT)			
	X	Y	Z	F	X	Y	Z	F
GO	0.02	-0.02	-0.04	–	0.29	0.24	0.0	–
CH	-0.08	0.01	0.01	-0.05	0.0	0.2	0.04	0.0
CR	0.09	0.0	0.12	0.28	0.43	0.21	0.36	0.81
GR	0.19	0.02	0.03	0.04	0.48	0.2	0.13	0.38
SW	-0.05	-0.02	-0.01	-0.09	0.0	0.0	0.16	0.0
OR	0.18	0.02	0.07	0.11	0.51	0.26	0.09	0.3

Table 4: Dimensionless and dimensional biases μ^* and μ fitted from the histograms of normalized residuals to ”core” field data with the PDF (14). See text for details.

C.2 For the external field

Dataset	c (nT)			
	X	Y	Z	F
GO	1.28	1.27	1.25	1.8
CH	1.17	1.62	1.49	1.63
CR	1.39	1.39	1.47	1.38
GR	1.33	1.23	1.37	1.56
SW	1.49	1.51	1.51	1.64
OR	1.45	1.34	1.36	1.8

Table 5: Optimized values of c (in nT) when fitting the dimensional residues to "core" field data with the PDF (14).

Dataset	μ^*				μ (nT)			
	X	Y	Z	F	X	Y	Z	F
CH	0.16	0.0	0.03	0.31	0.43	0.15	0.06	1.64
CR	-0.06	-0.1	0.0	0.31	0.0	0.0	0.0	2.33
GR	-0.07	0.04	0.01	0.14	0.0	0.44	0.16	1.76
SW	0.25	0.03	-0.01	0.27	0.75	0.26	0.0	1.11
OR	0.18	-0.06	0.03	0.13	0.99	0.0	0.05	1.11

Table 6: Dimensionless and dimensional biases μ^* and μ fitted from the histograms of normalized residuals to "core" minus "observed" field data with the PDF (14). See text for details.

Dataset	c (nT)			
	X	Y	Z	F
CH	1.82	1.52	1.27	2.29
CR	2.18	2.3	1.51	2.45
GR	2.18	1.09	1.41	2.06
SW	1.6	1.51	1.39	2.31
OR	1.28	1.83	1.37	1.83

Table 7: Optimized values of c (in nT) when fitting the dimensional residues to "core" minus "observed" field data with the PDF (14).